The Astrophysical Journal, 947:57 (13pp), 2023 April 20 https://doi.org/10.3847/1538-4357/acbf35

Shock Corrugation to the Rescue of the Internal Shock Model in Microquasars: The Single-scale Magnetohydrodynamic View

Patryk Pjanka[1], Camilia Demidem[1,2], and Alexandra Veledina[1,3]
[1] Nordita, Stockholm University and KTH Royal Institute of Technology, Hannes Alfvéns väg 12, SE-106 91 Stockholm, Sweden; patryk.pjanka@gmail.com
[2] JILA, University of Colorado and National Institute of Standards and Technology, 440 UCB, Boulder, CO 80309-0440, USA
[3] Department of Physics and Astronomy, FI-20014 University of Turku, Finland
Received 2022 November 15; revised 2023 February 22; accepted 2023 February 24; published 2023 April 20

Abstract

Questions regarding the energy dissipation in astrophysical jets remain open to date, despite numerous attempts to limit the diversity of the models. Some of the most popular models assume that energy is transferred to particles via internal shocks, which develop as a consequence of the nonuniform velocity of the jet matter. In this context, we study the structure and energy deposition of colliding plasma shells, focusing our attention on the case of initially inhomogeneous shells. This leads to the formation of distorted (corrugated) shock fronts—a setup that has recently been shown to revive particle acceleration in relativistic magnetized perpendicular shocks. Our study shows that the radiative power of the far downstream of nonrelativistic magnetized perpendicular shocks is moderately enhanced with respect to the flat-shock cases. Based on the decay rate of the downstream magnetic field, we make predictions for multiwavelength polarization properties.

Unified Astronomy Thesaurus concepts: Active galactic nuclei (16); X-ray binary stars (1811); Particle astrophysics (96); Magnetohydrodynamical simulations (1966); Shocks (2086); Jets (870)

1. Introduction

Fast relativistic outflows—jets—are common to astrophysical environments harboring accretion and/or explosions. Sources standing orders of magnitude apart in energy dissipation, such as young stellar objects, accreting black hole X-ray binaries, gamma-ray bursts, active galaxies, and blazars have all been witnessed launching such outflows (e.g., Goodson et al. 1997; MacFadyen & Woosley 1999; Mirabel & Rodríguez 1999). The mechanisms behind jet acceleration and fueling are, however, debated (Komissarov 2011; Davis & Tchekhovskoy 2020). Jets are known to produce bright nonthermal emission, often observed as power-law synchrotron and/or inverse Compton continua (e.g., see the review by Matthews et al. 2020), indicating continuously operating energy dissipation and particle acceleration mechanisms.

The jet kinetic energy can be converted to radiation via magnetic reconnection events (Lyutikov 2003), pair processes (Derishev et al. 2003; Stern & Poutanen 2008), or shocks in the interiors of the jets (Pe'er 2014). In the latter scenario, the jet is thought to be ejected as inhomogeneous matter, both in density and in velocity. This gives rise to discrete pockets of plasma (shells) traveling through the jet at different speeds. Once a faster shell catches up with a (previously ejected) slower one, they collide, and two shocks are formed (under the right conditions; see Pe'er 2014): a forward shock driven into the slower shell and a reverse shock driven into the faster one. These shocks could enable particle acceleration, and, consequently, power the nonthermal emission of the jet. After the collision, the shells are typically assumed to merge inelastically and continue propagating as a single shell (e.g., Beloborodov 2000; Malzac 2014; although see also Kino et al. 2004). They then encounter other shells and collide again, ensuring continuous particle reacceleration throughout the jet. This "internal shock model" was originally proposed in the context of the resolved inhomogeneous structures, the so-called "knots," in the jet of the M87 galaxy (Rees 1978). Later, the model was generalized to jets observed from other astrophysical sources: radio-loud quasars (Spada et al. 2001), gamma-ray bursts (Rees & Meszaros 1994; Medvedev & Loeb 1999; Beloborodov 2000), and microquasars (Kaiser et al. 2000; Malzac 2014).

Such bright knots have been observed in a number of sources, supporting localized energy dissipation scenarios (Matthews et al. 2020). The observed collision of these knots in the radio galaxy 3C 264 (Meyer et al. 2015) provided observational confirmation for the internal shock scenario in the context of active galactic nucleus (AGN) jets. In microquasars, internal shock models have proved to be successful in explaining both spectral and timing properties (Péault et al. 2019; Vincentelli et al. 2019). However, such modeling relies on a number of assumptions about energy liberation and particle acceleration in shell collisions, which need to be verified.

Different aspects of the flow structures and jet observables in the presence of internal shocks have been considered: the geometrical and hydrodynamic evolutions (Kino et al. 2004; Mimica et al. 2005; Granot 2012; Marino et al. 2020; Rudolph et al. 2020), thermodynamics (Kobayashi & Sari 2001; Mimica et al. 2004; Graff et al. 2008; Pe'er et al. 2017), the impacts of magnetic fields (Fan et al. 2004; Mimica et al. 2007; Mimica & Aloy 2010, 2012; Rueda-Becerril et al. 2014, 2015; Deng et al. 2015), radiative processes (Graff et al. 2008; Böttcher & Dermer 2010; Joshi & Böttcher 2011; Jamil & Böttcher 2012), and timing properties (Spada et al. 2001; Mimica et al. 2005; Böttcher & Dermer 2010; Jamil et al. 2010; Malzac 2013, 2014; Drappeau et al. 2015), among others. While the internal shock scenario is quite successful in representing a number of sources (e.g., Daigne & Mochkovitch 1998; Spada et al. 2001; Drappeau et al. 2015; Malzac et al. 2018; Péault et al. 2019;

Bassi et al. 2020; Marino et al. 2020), its main problem (and the main criticism of it) has to do with its apparent inefficiency in the energy conversion from kinetic to nonthermal particles (though this may depend on the model assumptions, as pointed out by Pe'er et al. 2017). It has been shown (Begelman & Kirk 1990; Sironi & Spitkovsky 2009, 2011) that electrons can consistently achieve nonthermal (power-law) distributions only in parallel shocks, where the magnetic field is nearly parallel to the shock normal. Once the obliquity of the magnetic field increases, particle acceleration is inhibited.

Recently, a potential solution to this issue has been proposed. Efficient particle acceleration can be recovered in the case of shocks that are corrugated (rippled) by upstream inhomogeneities (Demidem et al. 2022). Such inhomogeneities may be produced by inhomogeneous magnetic field configurations (e.g., Cerutti & Giacinti 2020) or as a result of kinetic turbulence (e.g., Zhdankin et al. 2017). Interestingly, such inhomogeneities have also been seen to self-consistently arise in kinetic electron–ion simulations (Ligorini et al. 2021). These findings can recover internal shocks as an efficient mechanism for producing nonthermal particles in relativistic outflows.

The structure behind (downstream of) shocks corrugated by upstream/downstream perturbations is much more complex than for planar shocks in homogeneous media. Demidem et al. (2018) described these perturbations in terms of eigenmodes of linear MHD (i.e., entropy, Alfvén, and magnetosonic waves) and studied the response of a fast perpendicular shock to each mode, one at a time. Their MHD simulations illustrate how an incoming upstream plane wave induces shock corrugation and is transmitted into a collection of modes in the downstream (see, e.g., their first figure or, for corrugation induced by the reflection of downstream perturbations, Figure 6 of Lyutikov et al. 2012). Demidem et al. (2022) used a kinetic approach (enabling the study of particle energization from first principles) and investigated the possible implications for particle acceleration in relativistic magnetized perpendicular shocks. While the process is inhibited for shocks in initially homogeneous media, they found that shock rippling and downstream turbulence induced by (upstream) harmonic density perturbations can lead to the generation of energetic particles.

Inspired by these results, the present work proposes to analyze the properties of a collision of 2D corrugated shells and how its observational signatures may differ from the idealized 1D case of flat shells. We perform relativistic MHD simulations of colliding shells, corrugated by ambient density or pressure inhomogeneities, and follow the evolutions of the density, magnetic field, and energy dissipation (as probed by synchrotron emission). We find that the quantities are moderately affected by the 2D structure of the shocks, relative to the 1D case with flat colliding shells. Hence, we conclude that the previous predictions of analytical models and hydrodynamic simulations hold for the case of acceleration-efficient corrugated shocks.

2. Methods

The 1D behaviors of colliding shells, including the effects of shell magnetization, initial internal energy, and other parameters, have been investigated in exquisite detail by previous works (e.g., Kobayashi & Sari 2001; Fan et al. 2004; Kino et al. 2004; Mimica et al. 2004, 2005, 2007; Jamil et al. 2010; Mimica & Aloy 2010, 2012; Joshi & Böttcher 2011; Pe'er et al. 2017; Rudolph et al. 2020). Thus, we treat the 1D behavior of the shells here as being well established, and instead focus on the difference between a 1D shell collision and the matching (see Section 2.4) 2D corrugated case.

In each (1D/2D) case, we simulate a collision of two identical dense shells, which are magnetized uniformly, with the magnetic field lines being perpendicular to their motion (corresponding to the so-called perpendicular shock configuration) and moving through a low-density unmagnetized ambient medium. We simulate the encounter in the zero-momentum frame of the system. For each test case, we run two simulations: a 1D one, with no shell structure perpendicular to the shell motion (Section 2.3), and a 2D one, with shell surface corrugation (Section 2.4).

2.1. Numerical Setup

We use the grid-based astrophysical MHD code `Athena 4.2`[4] (Stone et al. 2008), a Godunov code using the constrained transport method, to enforce the zero-divergence condition on magnetic fields.

Our simulations are performed in special relativistic MHD (Beckwith & Stone 2011), in Cartesian coordinates. The boundary conditions in the direction parallel to the shell motion (along the jet) are set as "free outflow" (the variables at the domain edge are copied to the ghost cells), while those perpendicular to the shell motion are periodic. The equation of state is adiabatic, with an adiabatic index of $\gamma_{\rm ad} = 4/3$. We use second-order reconstruction in primitive variables, the van Leer unsplit time integrator (Stone & Gardiner 2009), and HLLC (Toro 1999; Mignone et al. 2009) as our Riemann solver, with the Courant–Friedrichs–Lewy number (CFL) of 0.025.

For our grid resolution, we require that: (i) for each corrugation method (see Section 2.4), we resolve the corrugation width w of the shock by at least eight cells (parallel to the mean shock normal; see Section 2.5 and Figure 3); and (ii) that the resolution is nearly identical in both grid directions (i.e., our cells are nearly square-shaped). This results in a simulation resolution of 8192×1024 for a box of 40 light seconds $\times$ 6 light seconds (hereafter, lt-s). For the 1D simulations, we use the same resolution along the jet (for a fair comparison) and collapse the perpendicular direction to a single cell.

2.2. Choice of Parameter Space

To make our calculations more readable, we set our problem parameters and units to match the environment of an existing source (at least to an order of magnitude) and list them in Table 1. While our calculations are relevant for any relativistic jet where the emission is synchrotron-dominated, we provide numerical values for the microquasar GX 339−4. We briefly discuss a comparison with blazars, other prime candidates for the application of the internal shock model, at the end of this section.

GX 339−4 is a well-observed low-mass black hole X-ray binary, with a short duty cycle of X-ray outbursts of ∼2–3 yr (see, e.g., Corbel et al. 2013; Connors et al. 2019). While its orbital period can be measured precisely at 1.76 days (Hynes et al. 2003; Levine & Corbet 2006; Heida et al. 2017), the

[4] `Athena 4.2` is publicly available at https://github.com/PrincetonUniversity/Athena-Cversion. A fork of this repository, augmented to run and process the simulations presented in this paper, is available at https://github.com/ppjanka/Corrugated_internal_shocks.

Table 1
Parameters of Our Model

	Microphysics	
γ_{ad}	Adiabatic Index	4/3
	Geometry	
	Box size (lt-s)	40×6
	1D box size (cells)	8192×1
	2D box size (cells)	8192×1024
	Distance between shells (lt-s)	5
	Shell width (lt-s)	1
	Shell Fluid	
ρ_{sh}	Density	10^{-13} g cm^{-3}
σ	Magnetization	0.1
β	Plasma β	1
v_{sh}	Bulk speed (collision frame)	$0.1c$
	Ambient Medium	
ρ_{amb}	Density	$10^{-3}\ \rho_{sh}$
P_{amb}	Pressure	10^{-17}(g cm^{-3})c^2
B_{amb}	Magnetic field strength	0
	Synchrotron Flux	
D	Distance	8 kpc
R	Size of the emitting region (geometrical depth)	6×10^8 cm
Γ_j	Jet bulk Lorentz factor	2
i	Jet axis inclination	60° or $30° \sim 1/\Gamma_j$

Note. Where applicable, initial values are given—note that these may be altered by the corrugation procedure (for both the 1D and 2D runs; as explained in Section 2.4). For the synchrotron flux calculations, we use microquasar-relevant values as our fiducial model; we also discuss the application of our results to blazars in the text. c denotes the speed of light.

distance, compact object mass (and nature), and inclination are difficult to specify from observations. Heida et al. (2017) constrain these to the ranges of $D \gtrsim 5$ kpc, $M \in (2.3, 9.5) M_\odot$, and $i \in (37°, 78°)$, respectively. For the purpose of this work, we will adopt the values of $D \sim 8$ kpc and $M \sim 10\ M_\odot$. We also adopt a jet opening angle of $\theta_j \sim 2.°3$ and a jet bulk Lorentz factor of $\Gamma_j \sim 2$ (as assumed by Malzac et al. 2018—a value typical of microquasar jets; e.g., Tetarenko et al. 2019; Zdziarski et al. 2022b). We perform our calculations for two different inclinations: $i = 30° \sim 1/\Gamma_j$ (a head-on jet, corresponding to a blazar-like scenario) and $i = 60°$ (a jet seen from its side, more typical of X-ray binary jets). However, we find that the relative differences between corrugated and noncorrugated runs (on which we base our analysis; see Section 2.5) are very weakly dependent on inclination. Thus, we only report the results for $i = 60°$ in this manuscript.

If we scale our simulations to microquasar conditions, our region of interest would be radiating in the IR. Based on Malzac et al. (2018), this corresponds to $z \sim 10^3$–$10^6\ r_g$ (see their Figure 4), where $r_g = 1.5 \times 10^6$ cm for a black hole of $10 M_\odot$. Shidatsu et al. (2011) estimated the jet IR-emitting region size at $R \sim 6 \times 10^8$ cm. Assuming $\theta j = 2.°3$, this gives $z \sim 1.5 \times 10^{10}$ cm $\sim 10^4\ r_g$, which we adopt here.

In continuous jet models, applicable up to the radio-emitting regions far within the jet, it is often assumed that the high-energy particle and magnetic field energy densities are in equipartition (e.g., Hirotani 2005; Zdziarski et al. 2012; Drappeau et al. 2015; however, see also Zdziarski et al. 2015). For simplicity, we also follow this assumption here. To obtain the remaining plasma parameters, we use existing theoretical models of the binary from the literature to provide lower and upper constraints. We show the detailed derivations and the resulting ranges in the Appendix. Informed by these results, we adopt a rest-frame fluid density of $\rho \sim 10^{-13}$ g cm^{-3} and magnetization of $\sigma \sim 0.1$.

As noted above, while we report numerical values for a microquasar, our models can also be interpreted in terms of blazar sources. This would require a number of changes in Table 1, most of which would result in similar enhancements or decreases of synchrotron emission for both the 1D and 2D cases (i.e., changes of normalization). We are, however, only interested in the difference between the paired 1D/2D models. We find this difference to be mainly influenced by two parameters. Magnetization σ contains information about how dominant magnetic fields are in the dynamics of the problem. For large σ, magnetic fields are able to prevent corrugation, leading to the 1D and 2D results being more similar. Fortunately, the magnetization of the ballistic parts of a blazar jet can be estimated to $\sigma_\infty \sim 0.1$–0.01 (see Tchekhovskoy et al. 2009; Zdziarski et al. 2015, and references therein), so the conditions in blazar jets are similar to the ones presented here, in that respect. The second parameter of relevance is the bulk Lorentz factor of the jet Γ_j. Faster jets likely contain a broader distribution of shell speeds, with high-speed collisions (large v_{sh}) being more likely. In the models presented in our work, collisions are driven by the adiabatic expansion of the shells into the ambient medium between them. At faster relative speeds, this expansion may become less relevant to the collision outcome. If shell corrugation is caused by a pressure imbalance within the shell (see our pressure-corrugated runs; Section 2.4), this will result in flatter shocks and the 1D and 2D runs being more similar (i.e., with the corrugation having less effect in the synchrotron emission).

2.3. 1D Initial Conditions

Throughout the paper, the fluid quantities (density ρ and thermal pressure P) are given in the fluid rest frame, while the velocity v, Lorentz factor Γ, and magnetic field B are evaluated in the simulation frame (the zero-momentum frame of the shell collision). We denote the coordinate along the jet, parallel to the movement of the shells, as x, and the perpendicular one as y.

The initial conditions for the noncorrugated (1D) runs are depicted in Figure 1. The domain is composed of five regions, delimited by the shell edges x_{L1}, x_{L2} for the left shell and x_{R1}, x_{R2} for the right shell, with the subscript "1" being closer to the center of the domain and "2" being farther away. Note that our setup is symmetric, with respect to the plane of the (eventual) shell collision ($x = 0$, a vertical line at the center of our domain). Within the shells, the density is ρ_{sh}, the pressure is P_{sh}, the velocity v_{sh} is directed toward the center of the domain, and the magnetic field is set to $B_{sh}\boldsymbol{e}_y$. Outside the shells, the density equals ρ_{amb}, the pressure equals P_{amb}, and the magnetic field is 0. The velocity field in the ambient medium is

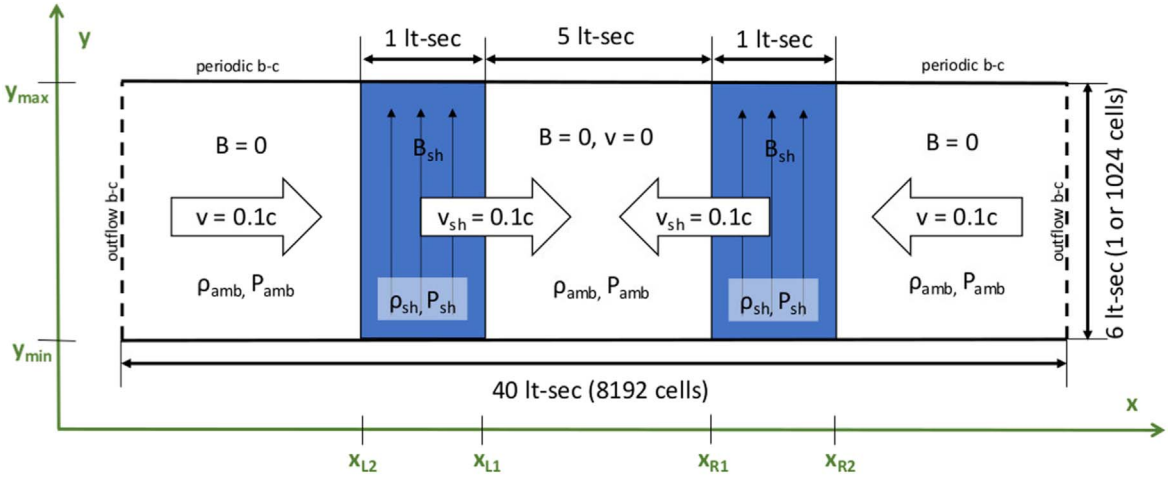

Figure 1. A diagram of our initial conditions and numerical setup (not to scale) before corrugation is applied.

initialized according to:

$$\boldsymbol{v} = \begin{cases} v_{\rm sh}\boldsymbol{e}_x, & x \leqslant x_{\rm L1}, \\ 0, & x \in (x_{\rm L1}, x_{\rm R1}), \\ -v_{\rm sh}\boldsymbol{e}_x, & x \geqslant x_{R1}. \end{cases} \tag{1}$$

Within the shells, the magnetic field strength $B_{\rm sh}$ and pressure $P_{\rm sh}$ are set through the plasma β and σ_B parameters:

$$B_{\rm sh} = \sqrt{8\pi\rho_{\rm sh}\sigma_{B,\rm sh}}\Gamma_{\rm sh}c, \tag{2}$$

$$P_{\rm sh} = \beta\frac{B_{\rm sh}^2}{8\pi\Gamma_{\rm sh}^2}. \tag{3}$$

Numerically, we set our initial conditions to $\rho_{\rm sh} = 10^{-13}\,{\rm g\,cm^{-3}}$, $\beta = 1$, $\sigma = 0.1$ (see Section 2.2 and Table 1), and $v_{\rm sh} = 0.1c$ (where c denotes the speed of light).

2.4. Shock Corrugation Methods

To produce the shock corrugation, we modulate the values of parameters from the previous paragraph in the direction perpendicular to the shell motion. In studies of corrugated shocks, various (typically dynamical) methods are used to induce the corrugation, or bending, of the shock front (see, e.g., Demidem et al. 2018). We investigate two possibilities: density and pressure modulation. In real astrophysical sources, such shock-rippling perturbations can follow very complex spatial dependencies. However, they can always be decomposed into harmonic components. Thus, as a first step, we use sinusoidal modulation to represent single harmonics of such shock-rippling density or pressure perturbations in the fluid, in a fashion similar to Demidem et al. (2018, 2022).

An important aspect of each implementation involves ensuring that each 1D/2D pair of simulations (with matching global parameters) is only distinguished by the 2D structure of the latter, and not by, e.g., the initial total synchrotron flux. As a result, each modulation in the initial conditions creating a 2D (corrugated) simulation may also include a change in the parameters of the corresponding 1D case (i.e., modifying its parameters: $\rho_{\rm amb}$, $\rho_{\rm sh}$, $P_{\rm amb}$, etc.). This is done to ensure that the initial lab-frame total energy (integrated over the simulation domain),

$$\epsilon_{\rm tot} = \int\left[\Gamma^2\left(\rho c^2 + \frac{\gamma_{\rm ad}}{\gamma_{\rm ad}-1}P\right) - P - \Gamma\rho c^2\right]dV, \tag{4}$$

shell momentum,

$$p_{\rm sh,tot} = \int_{\rm sh}\left[\Gamma^2\left(\rho c^2 + \frac{\gamma_{\rm ad}}{\gamma_{\rm ad}-1}P\right)\frac{v}{c^2}\right]dV, \tag{5}$$

and synchrotron power (see Section 2.5),

$$F_{\rm syn,tot} \propto B^{\frac{p+5}{2}}, \tag{6}$$

of the paired 1D/2D runs are identical (thus ensuring that the runs are comparable). In the equations above, Γ is the local fluid Lorentz factor (in the simulation frame), ρ is the local fluid-frame mass density, P is the fluid-frame thermal pressure, and B is the simulation-frame magnetic field strength. The conservation of quantities (4)–(6) can be achieved by ensuring that the averages of ρ, P, and B over the y-coordinate match between corresponding 1D/2D cases.

2.4.1. Density Modulation

In our first method of inducing shell corrugation, which we will refer to as "density corrugation," we change the density of ambient medium between the shells to exhibit "ridges" (sinusoidal density modulations that are oblique with respect to the shell surface) that bend the surface of each shell as it sweeps their mass. To ensure that the paired 1D run has initially identical global properties (4)–(6), we also increase the ambient medium density $\rho_{\rm amb}$ to match the mean density in the "ridged" zone in the 2D run. In other words, for the 2D case, we set:

$$\rho_{\rm 2D} = \begin{cases} \xi\rho_{\rm amb}, & x < x_{\rm L2}, \\ \rho_{\rm sh}, & x \in [x_{\rm L2}, x_{\rm L1}], \\ \rho_{\rm amb} + \frac{1}{2}(A_\rho\rho_{\rm sh} - \rho_{\rm amb}) \times \mathcal{M}_\rho(x, y), & x \in]x_{\rm L1}, x_{\rm R1}[, \\ \rho_{\rm sh}, & x \in [x_{\rm R1}, x_{\rm R2}], \\ \xi\rho_{\rm amb}, & x > x_{\rm R2}, \end{cases} \tag{7}$$

where A_ρ is the corrugation amplitude, $\xi = \frac{1}{2}\left(1 + A_\rho \frac{\rho_{\rm sh}}{\rho_{\rm amb}}\right)$, and

$$\mathcal{M}_\rho(x, y) = \cos\left(2\pi\left(n_x \frac{x - x_{\rm L1}}{x_{\rm R1} - x_{\rm L1}} + n_y \frac{y - y_{\rm min}}{y_{\rm max} - y_{\rm min}}\right)\right) + 1, \quad (8)$$

with $(n_x, n_y) = (1, 2)$. For the 1D case (to conserve the quantities in Equations (4) and (5)), we set

$$\rho_{\rm 1D} = \begin{cases} \xi\rho_{\rm amb}, & x < x_{\rm L2}, \\ \rho_{\rm sh}, & x \in [x_{\rm L2}, x_{\rm L1}], \\ \xi\rho_{\rm amb}, & x \in]x_{\rm L1}, x_{\rm R1}[, \\ \rho_{\rm sh}, & x \in [x_{\rm R1}, x_{\rm R2}], \\ \xi\rho_{\rm amb}, & x > x_{\rm R2}. \end{cases} \quad (9)$$

Note that we only adjust the ambient medium conditions, and leave the fluid within the shells unchanged. Thus, 1D/2D pairs of runs with different A_ρ have different density contrast ratios. While the runs with different A_ρ are in effect less easily comparable in absolute terms (and so we only use relative values in all our comparisons), it allows us to focus on the effect of corrugation.

Overall, we perform density corrugation simulations (1D/2D pairs) for A_ρ values of 0.01, 0.02, 0.05, 0.10, 0.20, 0.50, 0.75, and 1.00.

2.4.2. Shell Pressure Modulation

In the second method of inducing shell corrugation, henceforth referred to as "pressure corrugation," we implement a pressure modulation within the shell

$$P_{\rm sh,2D} = P_{\rm sh} + \frac{1}{2}A_P(P_{\rm sh} - P_{\rm amb}) \times \cos\left[2\pi\left(n_x \frac{x - x_{\rm S2}}{x_{\rm S1} - x_{\rm S2}} + n_y \frac{y - y_{\rm min}}{y_{\rm max} - y_{\rm min}}\right)\right], \quad (10)$$

where $S \in \{L, R\}$ is the shell index, $(n_x, n_y) = (1, 2)$, and A_P is the "corrugation amplitude." As the conditions in Equation (10) do not change our original mean internal energy, shell momentum, or synchrotron flux, the other initial conditions remain unchanged.

We perform pressure corrugation simulations (1D/2D pairs) for A_P values of 0.10, 0.20, 0.50, 0.75, and 1.00.

2.5. Diagnostics

2.5.1. Measuring Corrugation

In our models, shell corrugation is induced in the initial conditions, via the modulation fractions A_ρ and A_P. These parameters tell us little about the eventual shock geometry. Therefore, we explicitly measure the shape of the corrugated shock that we obtain in each simulation. As our diagnostic, we use the shock's "aspect ratio" (see Figure 2), the ratio of its width w—the distance between the maximum corrugation downstream and upstream—to its wavelength λ, set by the parameters $(n_x, n_y) = (1, 2)$ in Equations (8)–(10).

From the 1D version of a given run, we extract the maximal density for each frame, and note the time of maximal compression—which we consider to be the "collision time" $t_{\rm coll}$. For the 2D version, we inspect the frames between $t_{\rm coll} - t_{\rm cross}$ and $t_{\rm coll} + nt_{\rm cross}$ (with $n = 2$, 4 for the density and pressure corrugation runs, respectively), where $t_{\rm cross}$ is the light-crossing time of the initial shell width. For each or these frames, we measure the instantaneous shock width.

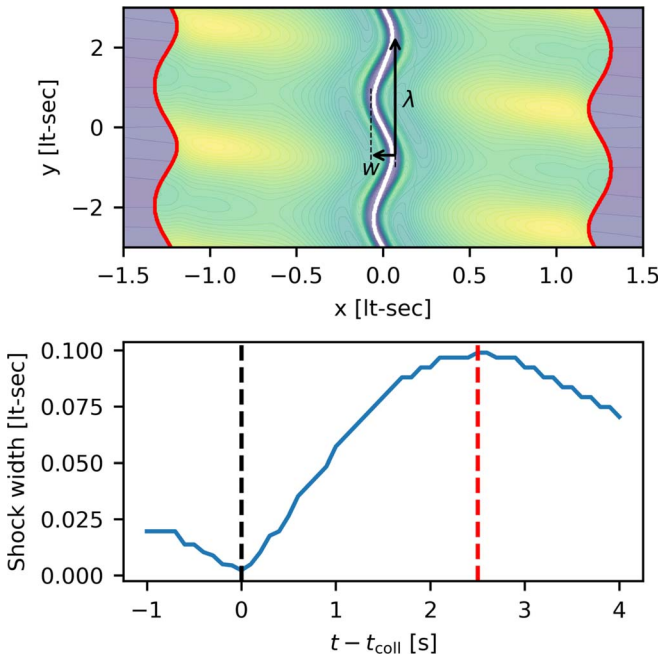

Figure 2. An example measurement of a shock corrugation aspect ratio ($a_{\rm sh} = w/\lambda$), for a pressure-corrugated case with $A_P = 0.2$. Top: a density contour plot, with the shock detections marked by the red lines and the aspect ratio measurement depicted by the white curve and annotations (see the text). Bottom: shock width w as a function of time (with respect to the collision time $t_{\rm coll}$). The dashed black and red lines show the moments of collision and maximal corrugation, respectively. The final shock width $w_{\rm max}$ is measured at the dashed red line.

1. In each frame, the center of the frame is surrounded on both sides by two shocks, either driven by shells propagating through the ambient medium ($t < t_{\rm coll}$) or driven into each shell by the collision ($t > t_{\rm coll}$). We localize these shocks using the velocity gradient. The x-coordinates of points with $|\partial v_x/\partial x|$ larger than a threshold value are averaged along the x-direction, separately for the left and right halves of the simulated domain, giving us the precise locations of both shocks at each y (shown by the red curves in Figure 2).
2. At each y, we average the x-position of these two shocks horizontally, to obtain the white stripe (along the center) in Figure 2.
3. We then collect the x-coordinates of all points within the white stripe (one per each y-value) and produce their histogram. To discard the outliers, we take the distance between the maxima of this histogram to be the width of the shock in a given frame.

In all our simulations, we find that the shock width as measured in this way decreases before the collision, reaches a minimum at $t_{\rm coll}$, then increases and reaches a maximum, after which the width continuously decreases as the postshock regions evolve. We take the postcollision maximal shock width $w_{\rm max}$ as the shock width for the given 1D/2D configuration (i.e., for the given A_ρ or A_P). The corrugation wavelength is

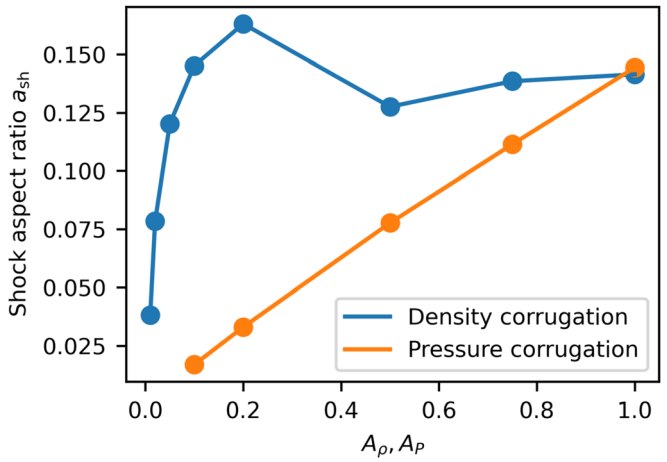

Figure 3. Scaling between the shock aspect ratio and the corrugation parameter of the initial conditions, for density corrugation (blue) and pressure corrugation (orange).

always $\Delta y/2$ (where Δy is the simulated box's height; see Equations (8)–(10)), giving us the aspect ratio of

$$a_{\rm sh} = 2w_{\rm max}/\Delta y. \tag{11}$$

We plot the relations between $a_{\rm sh}$ and A_ρ, A_P in Figure 3.

2.5.2. Synchrotron Emission

The main deliverable of internal shock models is their accurate prediction of the jet emission that, in the leptonic model adopted here, is powered by the nonthermal electron population. Of course, an MHD-only picture does not include nonthermal particles, and thus a number of assumptions must be adopted in order to extract the desired observables. We select our assumptions in line with typical prescriptions from the literature (see, e.g., Spada et al. 2001; Graff et al. 2008; Böttcher & Dermer 2010; Jamil et al. 2010; Malzac 2014; Rueda-Becerril et al. 2014; Malzac et al. 2018). At each location within the jet, the local nonthermal electron energy distribution is assumed to be a power law $dN/d\gamma \propto \gamma^{-p}$, with a slope of $p = 2.5$, extending between the Lorentz factors $\gamma_{\rm min} = 10$ and $\gamma_{\rm max} = 10^6$. Nonthermal electrons are taken to be in energy equipartition with the magnetic field (i.e., with the equipartition parameter $\zeta_e = U_e/U_B = 1$, where $U_e = \int\left(\gamma m_e c^2 \frac{dN}{d\gamma}\right)d\gamma$ and $U_B = B^2/(8\pi)$).

We stress that, as a consequence of the assumptions above, the impacts of thermal particles on the acceleration and radiative processes are assumed to be negligible—thermal particles (represented by the mass density in MHD simulations) only affect the fluid dynamics of the model. Particle acceleration is assumed to proceed until there is equipartition between the nonthermal particles and the magnetic field. Thus, the number density of the nonthermal particles is a direct function of the magnetic field energy density. This is regardless of the MHD mass density, which is assumed to be sufficiently large to provide seed particles for the nonthermal distribution, without being significantly depleted itself. In turn, we also assume that synchrotron emission and self-absorption are both completely dominated by nonthermal particles—we caution that this last assumption may not be applicable to some blazars, where self-absorption by thermal electrons may be important.

For our results, we report the synchrotron flux per unit of jet surface area in the observer's frame (e.g., Rybicki & Lightman 1979):

$$\frac{dF_\nu}{dS} = \frac{\delta^2 \Gamma_{\rm fl\to obs}}{2D^2} f_\nu \bar{I}_{\bar\nu}, \tag{12}$$

where $\delta = [\Gamma_{\rm fl\to obs}(1 - \boldsymbol{v}_{\rm fl\to obs}\cdot \boldsymbol{n}/c)]^{-1}$ is the Doppler factor, $\boldsymbol{n}$ is the direction toward the observer, $\Gamma_{\rm fl\to obs} = 1/\sqrt{1 - v^2_{\rm fl\to obs}/c^2}$, $f_\nu = 1$ is the volume filling factor of the nonthermal electrons, $\nu = \bar\nu\delta$ is the observer-frame photon frequency linked to the jet-frame frequency $\bar\nu$, and $\bar I_{\bar\nu}$ is the jet-frame synchrotron intensity. In order to determine the values of the fluid quantities in the observer's frame from their rest-frame values, one needs to account for both the velocity $\boldsymbol{v} = (v_x, v_y)$ of the fluid in the simulation frame (the zero-momentum frame of the shell collision) and the speed of the simulation frame in the observer frame $\boldsymbol{v}_{\rm j} = v_{\rm j}\boldsymbol{e}_x$ (the bulk velocity of the jet). We do so by performing Lorentz transformations of the fluid velocity:

$$\boldsymbol{v}_{\rm fl\to obs} = \frac{v_x + v_{\rm j}}{1 + v_x v_{\rm j}/c^2}\boldsymbol{e}_x + \frac{\sqrt{c^2 - v_{\rm j}^2}\, v_y}{c^2 + v_x v_{\rm j}}\boldsymbol{e}_y. \tag{13}$$

We consider the total IR–optical flux $dF_{\rm syn}/dS$, which we take to correspond to the flux integrated over the frequency range 300 GHz–3 PHz. For our assumed electron distribution, the local intensity can be written as (e.g., Rybicki & Lightman 1979; Beloborodov 2000; Malzac 2014):

$$\bar I_{\bar\nu} = \frac{j_{\bar\nu}}{\alpha_{\bar\nu}}(1 - e^{-\alpha_\nu R}), \tag{14}$$

where the synchrotron emission and extinction coefficients are:

$$j_{\bar\nu} = K_j \zeta_e B^{\frac{p+5}{2}} \bar\nu^{-\frac{p-1}{2}}, \tag{15}$$

$$K_j = \frac{\sqrt{3}\, e^3 i_\gamma}{16\pi^2 m_e^2 c^4 (p+1)} \times \Gamma\left(\frac{3p+19}{12}\right)\Gamma\left(\frac{3p-1}{12}\right)\left(\frac{m_e c}{3e}\right)^{-\frac{p-1}{2}}, \tag{16}$$

$$\alpha_{\bar\nu} = K_\alpha \zeta_e B^{\frac{p}{2}+3} \bar\nu^{-\frac{p+4}{2}} \tag{17}$$

$$K_\alpha = \frac{\sqrt{3}\, e^3 i_\gamma}{64\pi^2 m_e^3 c^4}\left(\frac{3e}{2\pi m_e c}\right)^{\frac{p}{2}} \times \Gamma\left(\frac{3p+2}{12}\right)\Gamma\left(\frac{3p+22}{12}\right), \tag{18}$$

where m_e and e are the electron mass and unit charge, respectively, and, for convenience, we define (following Malzac 2014):

$$i_\gamma^{-1} = \bar\gamma_e \int_{\gamma_{\rm min}}^{\gamma_{\rm max}} \gamma^{-p} d\gamma, \tag{19}$$

with $\bar\gamma_e$ being the mean electron Lorentz factor. For the optical depth $\alpha_{\bar\nu} R$, we select $R = 6\times 10^8$ cm, to match the size of the IR-emitting core of the jet (Shidatsu et al. 2011). In other words, we report our simulated box's flux as if it were located along the jet axis and observed via a line of sight at an angle of

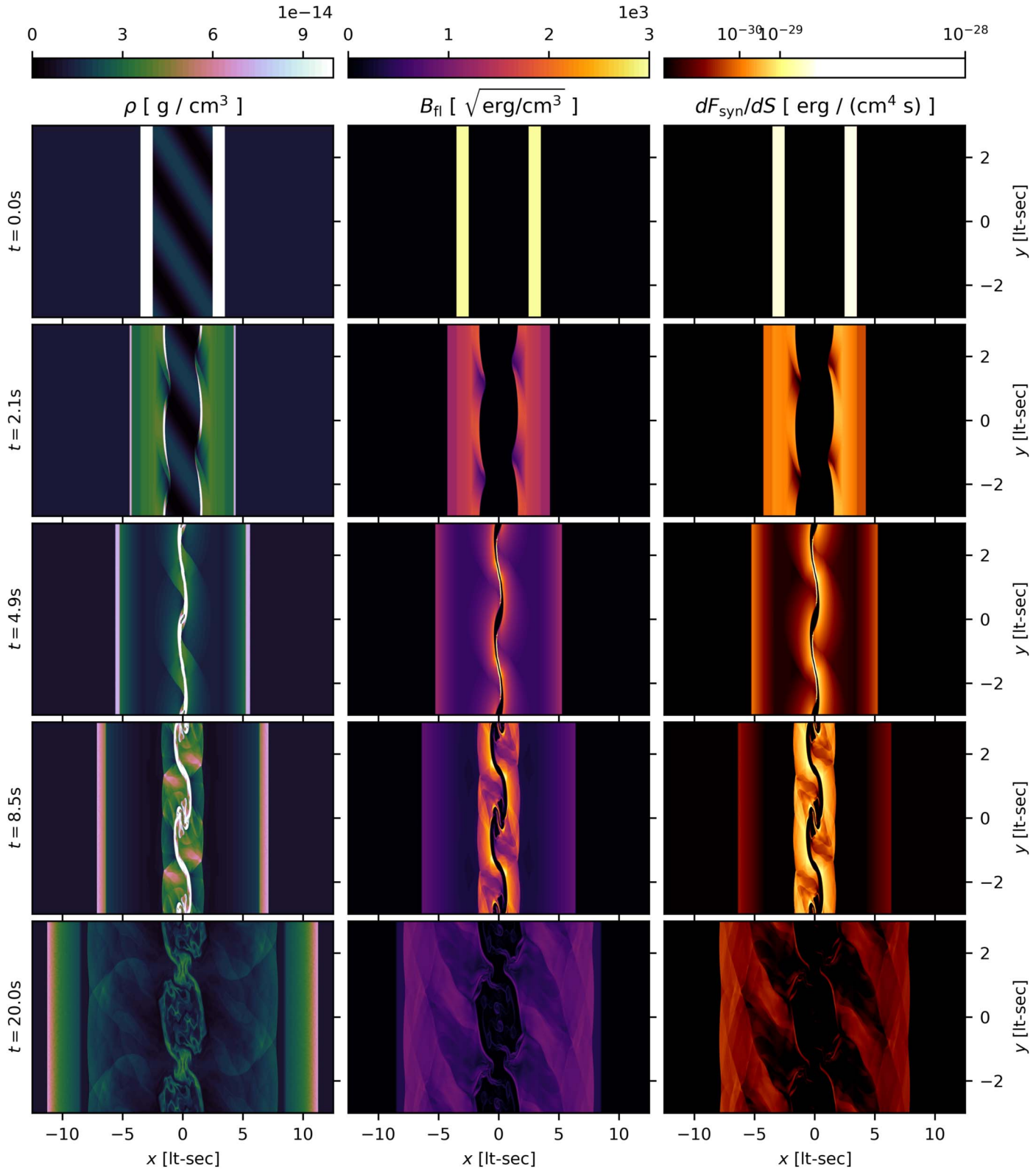

Figure 4. A representative selection of snapshots of the shell collision evolutions, taken from the density-corrugated (2D) simulation with $A_\rho = 0.2$, observed at the inclination of $i = 60°$. Left: fluid-frame density. Middle: fluid-frame magnetic field strength. Right: observer-frame synchrotron flux per unit of emitting surface (log-scale). Each row corresponds to a different time, as annotated on the left (see Figure 5). The linear and nonlinear evolutions of the shell corrugation can be seen with the progression of time. Note that, for the density corrugation case shown here, only the inner shell edges (the ones facing the other shell) are corrugated, while the outer shell edges remain flat, as they propagate outward into the ambient medium.

$1/\Gamma_j$ to the jet axis in the observer frame (i.e., perpendicular to the jet axis in the comoving frame).

3. Results

A typical sequence of events during one of the 2D simulations is shown in Figure 4. As the shells are overpressurized with respect to their surrounding ambient medium, the dynamics of the system is driven by the adiabatic expansion of the shells (for a thorough study of the dependence of shell collisions on the initial internal energy, see Pe'er et al. 2017). The shells start expanding into the ambient medium with speeds in excess of their bulk velocities, and evolve under the influence of the corrugation mechanism (see Section 2.4). Their surfaces ripple in a linear manner, resulting in near-sinusoidal shapes. As the shells collide, two shocks are driven into the shell material (one moving left, into the left shell, and one moving right, into the right one), and a thin line of (unmagnetized) compressed ambient medium is trapped at a contact discontinuity between the two postshock regions. The postshock material's density and magnetic field strength are both enhanced, with the latter causing strong synchrotron emission (see Section 3.1 for further details). Note that due to our assumption of energy equipartition between the nonthermal particles and the magnetic field, synchrotron emission is completely determined by the latter. As the collision material continues to evolve, it enters a nonlinear phase, during which the central part of the domain becomes disrupted. In the bottom two rows of Figure 4, the development of the Kelvin–Helmholtz instability can be seen at $x \sim 0$, to mediate this process. While the box-integrated total synchrotron flux remains high (albeit oscillating with time), the emission becomes spread over the growing postshock region, and the local flux density dims considerably (as seen in the bottom right corner of Figure 4).

3.1. Corrugation-driven Synchrotron Flux Enhancement

We investigate how corrugation affects the synchrotron flux from the shell collision site. Figure 5 shows the light curves integrated over our simulation boxes (top) and the relative differences between the synchrotron fluxes of the matched corrugated (2D) and noncorrugated (1D) cases (middle and bottom). We notice two effects introduced by shell corrugation.

There is a peak-then-dip pattern in the relative difference curves around the collision times (∼3–8 s). This is caused by the differences in the collision times. Due to corrugation, some regions of the 2D shell travel ahead of the 1D shell position, so the shells start colliding earlier in the corrugated (2D) case—thus giving more emission than the 1D case just before the 1D collision time (when the 2D collision happens), and less emission just afterward (which is at the 1D collision time, but already after the 2D collision peak).

A more interesting result is visible in the long-term behavior of the relative synchrotron flux differences. While the curves oscillate after the collision time, there is a clear overall enhancement of the synchrotron flux after the shell collision in the 2D case[5] —and this is especially visible for the pressure-corrugated case (the bottom row of Figure 5). To quantify this effect, we integrate the light curves over the simulation time, to obtain the total synchrotron emission (per unit surface) for each simulation. We then subtract the 1D from the 2D result, and divide by their mean, to obtain the total relative enhancement of the emission with respect to the 1D case. We plot these differences in Figure 6. We find that the differences can reach 14% in our parameter range. They also scale as a power law with the shock aspect ratio, with slopes of 1.5 ± 0.3 and 2.38 ± 0.02 for the density- and pressure-corrugated runs, respectively. Notably, the two curves for the density- and pressure-corrugated simulations match almost exactly. Therefore, the observed synchrotron enhancement is independent of the corrugation mechanism, and only sensitive to the actual shock geometry.

Under the approximations adopted to calculate the synchrotron flux from the MHD simulation output (namely, equipartition between the nonthermal particle and magnetic energy densities; see Section 2), the synchrotron flux depends only on the magnetic field. However, there are two ways in which the magnetic field structure can affect the emission. On one hand, an overall increase in the mean magnetic field strength will straightforwardly make the collision brighter. On the other hand, the synchrotron emission depends nonlinearly on the magnetic field strength (see Equation (6)). Thus, even if the mean magnetic field strength is identical between the 1D and 2D simulations, the presence of 2D structures in the latter can still alter the resulting synchrotron flux. To investigate which of these effects dominates in our case, we perform additional experiments. In a selected 2D run with well-visible synchrotron emission enhancement (the pressure-corrugated case with $A_P = 0.5$), we replace the magnetic field data with various modifications that deactivate some of the mechanisms above. The results are shown in Figure 7. The blue curve therein shows the original result, i.e., the 2D simulation with the original 2D magnetic field structure (compare with Figure 5). The orange curve corresponds to the same simulation, but we have replaced the original 2D magnetic field with the 1D result (i.e., the 1D magnetic field profile is replicated along the y-direction to fill the 2D simulation box). As this nullifies both of the mechanisms discussed—there is no change in the mean magnetic field and no 2D structure—this results in near-zero relative difference.[6] To obtain the green curve, we use the 2D magnetic field result, but scale it so that the mean value matches that of the 1D result. Thus, any enhancement in the mean value is removed, leaving only the influence of dimensionality (the 2D structure). We see that the resulting curve lies between the orange (with no $F_{\rm syn}$ enhancement) and blue (the actual 2D result) curves. Thus, the 2D nature of the magnetic field spatial distribution significantly contributes to the long-term synchrotron emission enhancement in corrugated simulations, but magnetic field amplification (which is stronger in corrugated than 1D shocks) has a comparable, if not slightly dominant, influence.

3.2. Downstream Magnetic Field Structure and Polarization Properties

Corrugation of the shock front affects the structure of the magnetic field in the downstream medium (see Figure 4 and

[5] Note that the outflow boundary conditions in the direction along the flow remain causally disconnected from the center throughout the simulation (and are therefore insensitive to the collision geometry). Thus, this is a genuine effect of corrugation, and not an artifact caused by boundary conditions.

[6] The remaining difference in the flux is due to the 2D velocity structure still being present after replacing the magnetic field data. The fluid velocity affects the transformation of magnetic fields from the observer frame (where the magnetic fields are defined) to the fluid frame (where we calculate synchrotron emission).

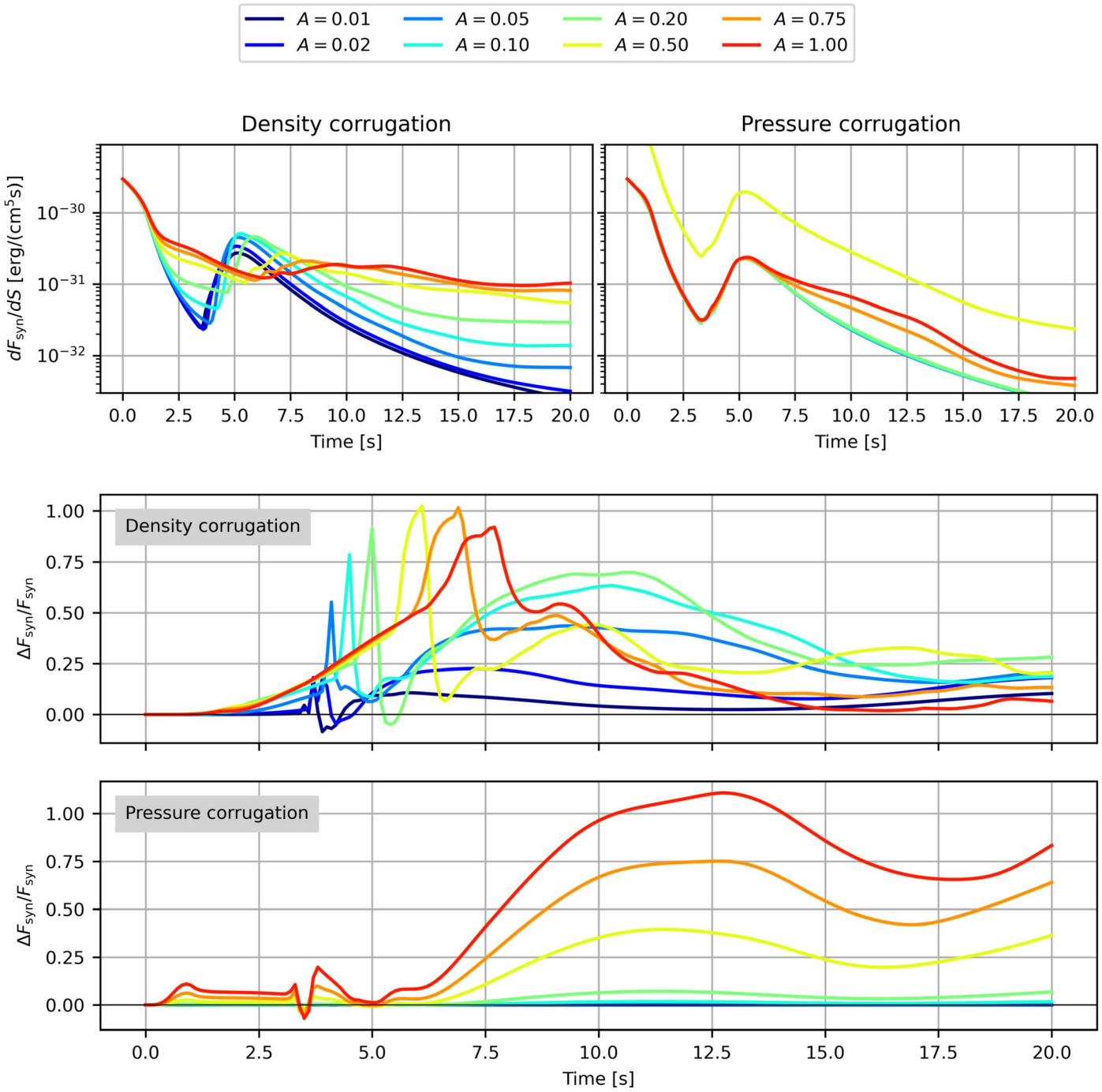

Figure 5. Top: light curves (mean synchrotron flux per surface emitting area) for all our simulations viewed at an inclination of $i = 60°$. Middle and bottom: the differences between the corrugated (2D) and noncorrugated (1D) matched simulations, shown as relative differences in synchrotron flux integrated over the whole simulation domain (i.e., $2(F_{\text{syn-tot,2D}} - F_{\text{syn-tot,1D}})/(F_{\text{syn-tot,2D}} + F_{\text{syn-tot,1D}})$). The curves are color-coded by the corrugation amplitudes A_ρ, A_P (see Figure 3 for the translation into shock aspect ratios).

Demidem et al. 2018). Information about the geometry of the magnetic field lines has been successfully extracted from observations using polarimetry. In this section, we investigate how the corrugated shell collisions affect the magnetic structure of the downstream and the multiwavelength polarimetric properties. Synchrotron polarization is orthogonal to the direction of the magnetic field, and it is expected to either be parallel or orthogonal to the jet direction for the cases of purely toroidal and poloidal configurations, respectively. In this respect, the ratio of the magnetic field components behind the shock front is of high importance. Previously, the dominance of the parallel field component was assumed at the shock front (Tavecchio et al. 2018), motivated by earlier studies of particle energization possibilities at shock fronts (Sironi & Spitkovsky 2009; Sironi et al. 2013). Tavecchio et al. (2018) found that the observed polarization fractions of optical and X-ray emission in BL Lacertae jets could be deduced from the slope of the power law fitting the decay of the shock-perpendicular magnetic field $B_\perp$ (the component parallel to the shock front, i.e., perpendicular to the shock normal) behind the shock.

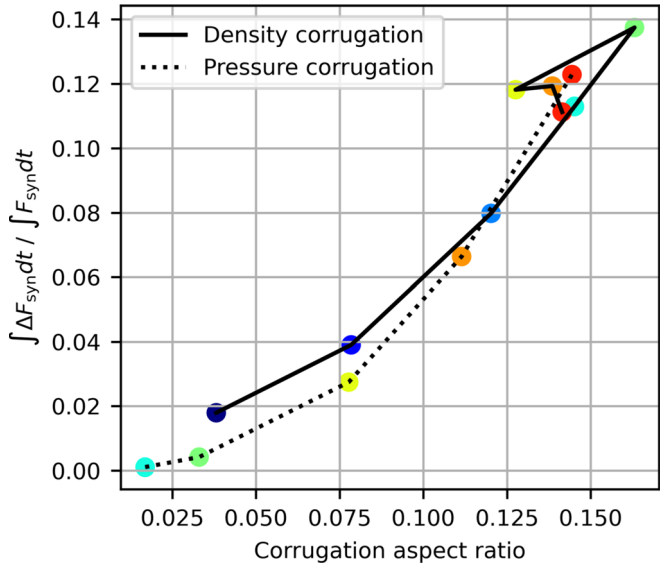

Figure 6. The effect of corrugation on the total synchrotron emission, shown by the dependence of the relative difference in the total synchrotron emission (i.e., flux integrated over the simulated domain and simulation time) between the corrugated (2D) and noncorrugated (1D) cases, as a function of the shock aspect ratio (see Section 2.5 and Figure 3). The point colors match the corresponding curves for each run and corrugation method in Figure 5. Note that as a ratio of the synchrotron fluxes, this relation is independent of the viewing inclination.

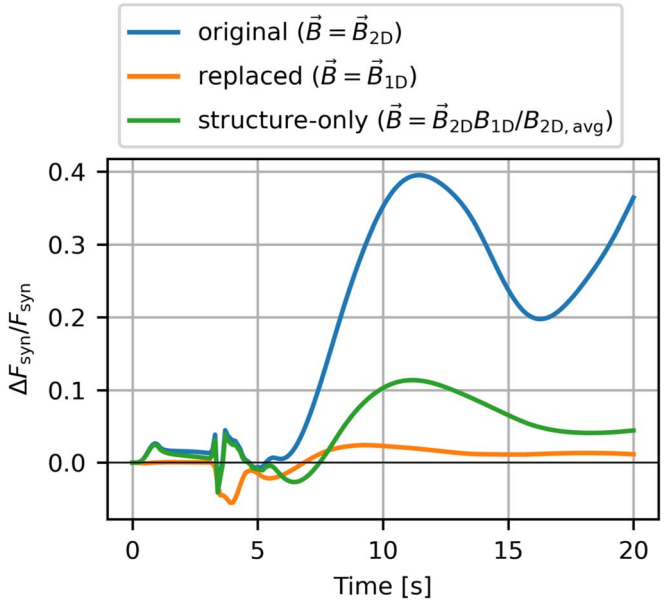

Figure 7. Investigation of the cause of long-term synchrotron emission enhancement. The curves show the relative synchrotron enhancement for the corrugated (2D) simulation with respect to the matched uncorrugated one (1D; see the bottom panels of Figure 5), for the pressure-corrugated case with $A_P = 0.5$. To calculate the emission in the corrugated case, the magnetic field was either kept unchanged (blue curve), replaced with the magnetic field from the uncorrugated (1D) case (orange curve), or the value was scaled down, so that the mean magnetic field strength matched that of the 1D simulation, with the 2D structure left unchanged (green curve). It can be seen that both the 2D structure and an overall magnetic field enhancement contribute to the enhanced synchrotron emission for the corrugated shell collisions.

In their analysis, Tavecchio et al. (2018) assumed the preshock magnetic field to be composed of a shock-parallel component (along the flow direction/shock normal) following a well-defined profile, and a randomly oriented shock-perpendicular component. In this work, we consider a homogeneous shock-perpendicular configuration. However, the postshock magnetic field strength is always locally dominated by the compressed shock-perpendicular component (randomly oriented, in the case of Tavecchio et al. 2018; see their Figure 3). Thus, the postshock region of our model can be viewed as a small region of the postshock domain of Tavecchio et al. (2018), where the magnetic field can be treated as homogeneous.

Given these considerations, we can measure the decay slopes of $B_\perp$ in our simulations, and discuss what they imply for the measured polarization in light of the study by Tavecchio et al. (2018). After finding shock positions using the local maxima of $|\partial B_\perp/\partial x|$, we plot the y-averaged $B_\perp$ as a function of distance from the shock in Figure 8. Since each simulation contains two shocks (in the left and right shells), the average between the two is used.

We find that $B_\perp$ remains constant close to the shock, then drops, approximately as a power law. This structure indicates that there is a rarefaction trailing each shock, with a near-homogeneous fluid between them. Due to the fact that the ambient medium between the shells (through which the rarefaction travels) is adjusted between runs for the density corrugation case (see Section 2.4), we observe much greater diversity in the curve shapes there (top row of Figure 8), while the runs for the pressure corrugation case (bottom row of Figure 8) all behave similarly. In each case, the behaviors of the matching 1D and 2D runs are very similar, showing that the quantities linear in B, such as the mean $B_\perp$ considered here, are well approximated by the solution to the 1D Riemann problem.

A (hard) broken power-law fit to $B_\perp(x - x_{sh})$ yields the results presented in the right column of Figure 8. We see that the postshock power-law slope remains within the range $[-0.50, -0.15]$ for the density-corrugated simulations, and is well constrained at ~ -0.14 for the pressure-corrugated ones. Tavecchio et al. (2018) find that the slope (in their notation, $-m$; see their Figure 4) of ~ -0.4 results in high polarization fractions for both the optical and X-ray bands, with the latter being somewhat higher than the former, $\gtrsim$45% versus $\sim$33%. We caution that these specific values would only apply to the case of a single-shell collision. Once a lot of events overlap (with some collisions likely being off-center, at different inclinations to the jet axis), the expected total polarization fraction of the jet emission should be lower, and could be comparable to the X-ray polarization recently detected by the Imaging X-ray Polarimetry Explorer (IXPE; Liodakis et al. 2022). Nonetheless, unless another source of polarized radiation contributes to the observed bands, the X-ray emission should remain more strongly polarized than the optical band.

4. Discussion and Conclusions

In this paper, we revise the viability of internal shock collisions for powering the emission of relativistic jets. Given a sufficient presence of high-energy particles, the synchrotron emission in these environments is largely dictated by the strength and orientation of the magnetic fields (see the discussion in Section 2). At the base of the jet, these may be randomly, or even poloidally, oriented (Vlahakis & Königl 2003; Komissarov et al. 2009; Zdziarski 2022a). However, the magnetic fields parallel ($B_\parallel$) and perpendicular ($B_\perp$) to the jet axis evolve differently with the distance from the

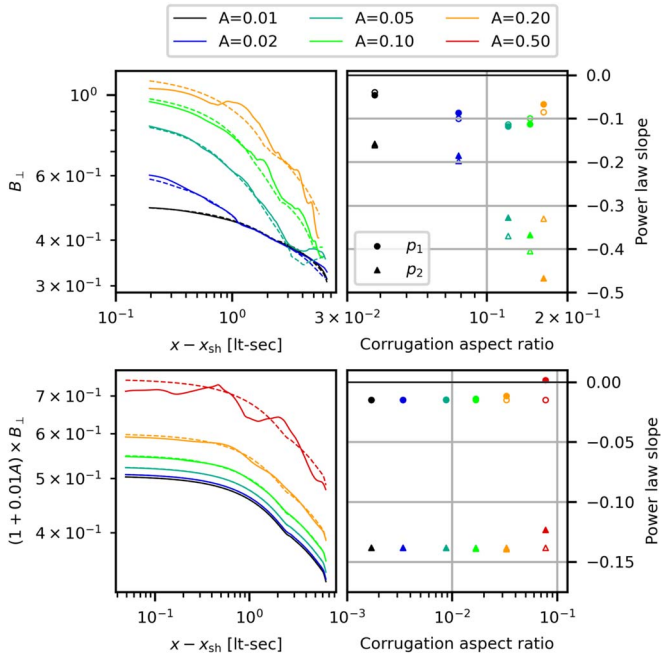

Figure 8. Decay of the magnetic field component perpendicular to the shock normal, $B_\perp$. Left: $B_\perp$ as a function of the distance from the shock front, $x - x_{sh}$. The solid lines show the vertically averaged values from the 2D simulations, while the dashed lines show the values from the 1D runs. Right: slopes of the two power laws fit to the measurements (p_1—close to the shock front; p_2—farther away), as a function of the corrugation aspect ratio. The open and solid symbols refer to the fits to the 1D and 2D results, respectively. The top row presents the results for the density corrugation simulations, while the bottom row shows the pressure corrugation results. All the curves and markers are color-coded by the simulation amplitudes, as indicated in the legend.

central engine (Blandford & Königl 1979):

$$B_{||} \propto z^{-2} (\text{magnetic flux conservation}),$$
$$B_\perp \propto z^{-1} (\text{magnetic energy conservation}). \quad (20)$$

This causes the magnetic field to be predominantly toroidal in the radio-emitting parts of the jet (as evidenced by observations of the radio and optical polarization of blazars; e.g., Gabuzda & Cawthorne 2000; Gabuzda et al. 2006; Walker et al. 2018; Issaoun et al. 2022; Zhao et al. 2022).

Internal shocks are driven along the jet axis into this changing configuration of magnetic fields. Close to the central engine, where $\boldsymbol{B}$ is randomly or poloidally oriented, this may result in quasi-parallel shocks (with $\boldsymbol{B}$ nearly parallel to the shock normal), which are known to be efficient particle accelerators in the standard diffusive shock acceleration mechanism (Sironi & Spitkovsky 2009; Sironi et al. 2015a). Farther away, the internal shocks likely become nearly exclusively perpendicular (with $\boldsymbol{B}$ perpendicular to the shock normal)—a configuration that has long been considered inefficient for particle acceleration (Begelman & Kirk 1990; Sironi et al. 2013). This prompted efforts considering alternative particle energization mechanisms, such as magnetic reconnection (Sironi et al. 2015b). It has recently been found that perpendicular shocks may lead to particle acceleration when their surface is corrugated (Demidem et al. 2022). Such a situation is not unlikely. Turbulence and density inhomogeneities within the jet can easily affect the shock structure, either directly, or through secondary instabilities (as has been shown for gamma-ray burst models; e.g., López-Cámara et al. 2016; Gottlieb et al. 2020).

While corrugation offers a way of producing suprathermal particles in quasi-perpendicular magnetized shocks—a natural configuration for the internal shocks in jets—its net effect on the downstream structure and radiative properties has not previously been investigated. Here, we assess whether the current phenomenological approach to computing the spectral and timing properties of the internal shock model, which assumes 1D collisions in its emission calculations (e.g., Beloborodov 2000; Malzac 2014; Marino et al. 2020), is still valid in the less trivial and arguably more realistic case of corrugated shocks.

Assuming in both cases that particles attain a power-law energy distribution, we find the corrugated shocks to be up to $\sim$10% brighter than their flat counterparts. We acknowledge this to be a small correction, in comparison to the effects of other approximations that are made in internal shock models. Thus, we conclude that the existing internal shock models are entirely consistent with the behavior of 2D corrugated shocks, at least in the simplified MHD approach presented here. We caution that a detailed treatment of the particle acceleration resulting from corrugated shocks (either through test particles or particle-in-cell simulations) may well change this conclusion.

It is well known that multiwavelength polarization studies reveal the structure of the magnetic fields in jets (e.g., Gabuzda & Cawthorne 2000; Gabuzda et al. 2006; Issaoun et al. 2022). With the recent launch of IXPE (Weisskopf et al. 2022), studies have been able to reach the regions immediately behind the shock fronts, for the first time. Our simulations allow us to make predictions regarding the level of polarization of the jet synchrotron emission in the context of internal shock models.

From the point of view of a single-shell collision, our results allow us to apply the findings of Tavecchio et al. (2018), leading to the prediction that a single two-shell collision in the region of the toroidal magnetic field (far within the jet) should result in low optical and high X-ray polarization fractions. At the same time, a similar collision close to the central engine would occur at a much higher value of $B_{||}$ (as discussed above), resulting in highly polarized radiation in both spectral regions. However, the frequency of the peak of the synchrotron emission flux depends on the distance from the central engine ($\nu \propto z^{-1}$, known as "core-shift"; Lobanov 1998; Hirotani 2005), so the regions close to the accretion disk will mainly radiate in X-rays, while those farther out will be seen in optical/IR/radio bands. Thus, we can predict, overall, that the jet-integrated synchrotron emission from an internal-shock–powered jet should exhibit a highly polarized X-ray emission and a weakly polarized optical/IR emission. We are excited to see these expectations systematically investigated with multi-wavelength polarimetric data.

Our work expands the 1D picture of shell collisions, which is typically used for internal shock models, into 2D. A natural next step would be to investigate a fully 3D system. Instabilities may behave differently in 2D than in 3D. However, the only instability that we observe in our runs is the Kelvin–Helmholtz instability, which, by its nature, remains locally 2D. As reported by, e.g., Markwick et al. (2021), colliding flows may also exhibit radiative instabilities that do evolve differently in 3D. Still, due to the small radiative power of microquasar/AGN jets relative to their kinetic power, these instabilities

should not have significant dynamical consequences on our systems of interest. Thus, we expect the downstream behavior in 3D to be similar to that in 2D. The main finding of our 2D work is that the magnetic field is amplified in structured (as opposed to 1D) systems, leading to brighter synchrotron emission. It is difficult to say whether this amplification would be stronger or weaker in 3D configurations. However, a dynamo may operate in 3D, in addition to the process that we observe here, leading to further amplification of the magnetic fields. Thus, we expect the increase in synchrotron brightness in 3D to be comparable to or even larger than that in 2D. Further work in 3D would be needed to address whether the conjectures that we list above are correct.

This research was performed with computing resources (Beskow, Dardel) that were generously provided by the PDC Center for High Performance Computing at the KTH Royal Institute of Technology, allocated through the Swedish National Infrastructure for Computing (SNIC). Nordita is supported in part by NordForsk. C.D. acknowledges support from NSF grant AST 1903335 and NASA grant NNX17AK55G. A.V. acknowledges support from Academy of Finland grant Nos. 309308 and 322779.

Appendix
Parameter Range Estimation for the GX 339−4 Environment

To obtain plasma parameters close to those expected for GX 339−4, we use existing theoretical models of the binary from the literature to provide lower and upper constraints on the values of interest, then select values within the resulting ranges.

Lower limits. Maitra et al. (2009) calculate the particle density of the leptons at the jet ejection zone of GX 339−4 to be

$$n_{\rm e}(r_{\rm ej}) \sim 4 \times [10^{13.4}, 10^{15}]\,{\rm cm}^{-3} \gtrsim 10^{14}\,{\rm cm}^{-3}, \tag{A1}$$

where the factor of 4 comes from the transformation to the postshock density. The location of the ejection region is constrained within (their Table 2)

$$z_{\rm ej} \sim 33 - 114 r_{\rm g}. \tag{A2}$$

Here, we will assume the jet to be roughly conical between the ejection zone and the IR zone of Shidatsu et al. (2011), at $\sim 10^4$ $r_{\rm g}$. As the jet is likely convex while accelerating, this will likely underestimate the local particle number density:

$$n_{\rm e}(z) \propto z^{-2}, \tag{A3}$$

$$n_{\rm e}(z_{\rm IR}) \gtrsim 1.3 \times 10^{10}\,{\rm cm}^{-3}. \tag{A4}$$

This gives us the local mass density

$$\rho(z_{\rm IR}) \gtrsim n_{\rm e} m_{\rm p} \sim 4.2 \times 10^{-14}\,{\rm g\,cm}^{-3}, \tag{A5}$$

and the magnetization

$$\sigma_{\rm j}(z_{\rm IR}) \simeq \frac{B^2/8\pi}{\rho(z_{\rm IR})c^2} \lesssim 2.6. \tag{A6}$$

We can also calculate the plasma skin depth:

$$l_{\rm s} = \frac{c}{\omega_{pe}} = c\sqrt{\frac{m_e}{4\pi n_{\rm e} e^2}} \lesssim 3.4\,{\rm cm}. \tag{A7}$$

Upper limits. As argued by Maitra et al. (2009), the total jet power $P_{\rm j}$ is larger than the bulk kinetic energy advection in protons by a factor of $\sim$10, as it also contains the energy that is used later to reheat the particle distribution (by, e.g., internal shocks; see the discussion in their Section 2.1 regarding the "input power parameter" $N_{\rm j}$ and its relation to the total jet power of Markoff et al. 2005). Interestingly, their $N_{\rm j}$ (see their Table 2) is actually very close in value to the $P_{\rm j}$ from Malzac et al. (2018; however, as these are physically different models, this observation need not necessarily be meaningful). Given these findings, as well as the results regarding the jet power from Gallo et al. (2005) and Bright et al. (2020), the local plasma parameters can be estimated by lowering the jet power $P_{\rm j}$ of Malzac et al. (2018) by a factor of 10. Thus, in this paragraph, we will take $P_{\rm j} \sim 10^{37}\,{\rm erg\,s}^{-1}$.

Assuming that the jet power is fully dominated by the kinetic energy of protons (i.e., overestimating the jet power),

$$P_{\rm j} \lesssim (\Gamma_{\rm j} - 1)\rho c^2 \times v_{\rm j} \times \pi(\theta_{\rm j} z)^2, \tag{A8}$$

$$\rho(z) \lesssim \frac{P_{\rm j}}{(\Gamma_{\rm j} - 1) v_{\rm j} c^2 \times \pi(\theta_{\rm j} z)^2}, \tag{A9}$$

$$\sigma_{\rm j}(z) \gtrsim \frac{B^2 (\Gamma_{\rm j} - 1) v_{\rm j} \times \pi(\theta_{\rm j} z)^2}{8\pi P_{\rm j}}. \tag{A10}$$

This, for the location of the IR core from Shidatsu et al. (2011), gives us:

$$\rho(z_{\rm IR}) \lesssim 4.3 \times 10^{-13}\,{\rm g\,cm}^{-3}, \tag{A11}$$

$$\sigma_{\rm j}(z_{\rm IR}) \gtrsim 0.25. \tag{A12}$$

Note that this is given in the frame of reference comoving with the jet at its bulk Lorentz factor, $\Gamma_{\rm j} \sim 2$.

Assuming charge neutrality, we can obtain the electron number density in this frame from the mass density above:

$$n_{\rm e} \simeq \rho(z)/m_{\rm p} \gtrsim 2.6 \times 10^{11}\,{\rm cm}^{-3}. \tag{A13}$$

This gives a plasma skin depth of

$$l_{\rm s} = \frac{c}{\omega_{pe}} = c\sqrt{\frac{m_e}{4\pi n_{\rm e} e^2}} \lesssim 1.0\,{\rm cm}. \tag{A14}$$

Combined constraints. Based on the considerations above, we can constrain the fluid parameters within the GX 339−4 jet to be within the following ranges:

$$\rho \in [4.2 \times 10^{-14}, 4.3 \times 10^{-13}]\,{\rm g\,cm}^{-3}, \tag{A15}$$

$$n_{\rm e} \in [1.3 \times 10^{10}, 2.6 \times 10^{11}]\,{\rm cm}^{-3}, \tag{A16}$$

$$\beta \sim 1, \tag{A17}$$

$$\sigma \in [2.6, 0.25], \tag{A18}$$

$$l_s \in [3.4, 1.0]\ \mathrm{cm}, \tag{A19}$$

where ρ denotes the density, n_e denotes the electron number density, β denotes the plasma beta (defined as the ratio of the particle to magnetic field energy density), σ denotes the magnetization, and l_s is the plasma skin depth. Note that we have $\sim 10^8$–10^9 of local skin depths per jet radius at our region of interest, at $z_{IR} \sim 10^4\ r_g$.

ORCID iDs

Patryk Pjanka https://orcid.org/0000-0003-3564-9689
Camilia Demidem https://orcid.org/0000-0003-3433-0772
Alexandra Veledina https://orcid.org/0000-0002-5767-7253

References

Bassi, T., Malzac, J., Del Santo, M., et al. 2020, MNRAS, 494, 571
Beckwith, K., & Stone, J. M. 2011, ApJS, 193, 6
Begelman, M. C., & Kirk, J. G. 1990, ApJ, 353, 66
Beloborodov, A. M. 2000, ApJL, 539, L25
Blandford, R. D., & Königl, A. 1979, ApJ, 232, 34
Böttcher, M., & Dermer, C. D. 2010, ApJ, 711, 445
Bright, J. S., Fender, R. P., Motta, S. E., et al. 2020, NatAs, 4, 697
Cerutti, B., & Giacinti, G. 2020, A&A, 642, A123
Connors, R. M. T., van Eijnatten, D., Markoff, S., et al. 2019, MNRAS, 485, 3696
Corbel, S., Coriat, M., Brocksopp, C., et al. 2013, MNRAS, 428, 2500
Daigne, F., & Mochkovitch, R. 1998, MNRAS, 296, 275
Davis, S. W., & Tchekhovskoy, A. 2020, ARA&A, 58, 407
Demidem, C., Lemoine, M., & Casse, F. 2018, MNRAS, 475, 2713
Demidem, C., Nättilä, J., & Veledina, A. 2022, arXiv:2212.06053
Deng, W., Li, H., Zhang, B., & Li, S. 2015, ApJ, 805, 163
Derishev, E. V., Aharonian, F. A., Kocharovsky, V. V., & Kocharovsky, V. V. 2003, PhRvD, 68, 043003
Drappeau, S., Malzac, J., Belmont, R., Gandhi, P., & Corbel, S. 2015, MNRAS, 447, 3832
Fan, Y. Z., Wei, D. M., & Zhang, B. 2004, MNRAS, 354, 1031
Gabuzda, D. C., & Cawthorne, T. V. 2000, MNRAS, 319, 1056
Gabuzda, D. C., Rastorgueva, E. A., Smith, P. S., & O'Sullivan, S. P. 2006, MNRAS, 369, 1596
Gallo, E., Fender, R., Kaiser, C., et al. 2005, Natur, 436, 819
Goodson, A. P., Winglee, R. M., & Böhm, K.-H. 1997, ApJ, 489, 199
Gottlieb, O., Levinson, A., & Nakar, E. 2020, MNRAS, 495, 570
Graff, P. B., Georganopoulos, M., Perlman, E. S., & Kazanas, D. 2008, ApJ, 689, 68
Granot, J. 2012, MNRAS, 421, 2467
Heida, M., Jonker, P. G., Torres, M. A. P., & Chiavassa, A. 2017, ApJ, 846, 132
Hirotani, K. 2005, ApJ, 619, 73
Hynes, R. I., Steeghs, D., Casares, J., Charles, P. A., & O'Brien, K. 2003, ApJL, 583, L95
Issaoun, S., Wielgus, M., Jorstad, S., et al. 2022, ApJ, 934, 145
Jamil, O., & Böttcher, M. 2012, ApJ, 759, 45
Jamil, O., Fender, R. P., & Kaiser, C. R. 2010, MNRAS, 401, 394
Joshi, M., & Böttcher, M. 2011, ApJ, 727, 21
Kaiser, C. R., Sunyaev, R., & Spruit, H. C. 2000, A&A, 356, 975
Kino, M., Mizuta, A., & Yamada, S. 2004, ApJ, 611, 1021
Kobayashi, S., & Sari, R. 2001, ApJ, 551, 934
Komissarov, S. S. 2011, MmSAI, 82, 95
Komissarov, S. S., Vlahakis, N., Königl, A., & Barkov, M. V. 2009, MNRAS, 394, 1182
Levine, A. M., & Corbet, R. 2006, ATel, 940, 1
Ligorini, A., Niemiec, J., Kobzar, O., et al. 2021, MNRAS, 501, 4837
Liodakis, I., Marscher, A. P., Agudo, I., et al. 2022, Natur, 611, 677
Lobanov, A. P. 1998, A&A, 330, 79
López-Cámara, D., Lazzati, D., & Morsony, B. J. 2016, ApJ, 826, 180
Lyutikov, M. 2003, NewAR, 47, 513
Lyutikov, M., Balsara, D., & Matthews, C. 2012, MNRAS, 422, 3118
MacFadyen, A. I., & Woosley, S. E. 1999, ApJ, 524, 262
Maitra, D., Markoff, S., Brocksopp, C., et al. 2009, MNRAS, 398, 1638
Malzac, J. 2013, MNRAS, 429, L20
Malzac, J. 2014, MNRAS, 443, 299
Malzac, J., Kalamkar, M., Vincentelli, F., et al. 2018, MNRAS, 480, 2054
Marino, A., Malzac, J., Del Santo, M., et al. 2020, MNRAS, 498, 3351
Markoff, S., Nowak, M. A., & Wilms, J. 2005, ApJ, 635, 1203
Markwick, R. N., Frank, A., Carroll-Nellenback, J., et al. 2021, MNRAS, 508, 2266
Matthews, J. H., Bell, A. R., & Blundell, K. M. 2020, NewAR, 89, 101543
Medvedev, M. V., & Loeb, A. 1999, ApJ, 526, 697
Meyer, E. T., Georganopoulos, M., Sparks, W. B., et al. 2015, Natur, 521, 495
Mignone, A., Ugliano, M., & Bodo, G. 2009, MNRAS, 393, 1141
Mimica, P., & Aloy, M. A. 2010, MNRAS, 401, 525
Mimica, P., & Aloy, M. A. 2012, MNRAS, 421, 2635
Mimica, P., Aloy, M. A., & Müller, E. 2007, A&A, 466, 93
Mimica, P., Aloy, M. A., Müller, E., & Brinkmann, W. 2004, A&A, 418, 947
Mimica, P., Aloy, M. A., Müller, E., & Brinkmann, W. 2005, A&A, 441, 103
Mirabel, I. F., & Rodríguez, L. F. 1999, ARA&A, 37, 409
Péault, M., Malzac, J., Coriat, M., et al. 2019, MNRAS, 482, 2447
Pe'er, A. 2014, SSRv, 183, 371
Pe'er, A., Long, K., & Casella, P. 2017, ApJ, 846, 54
Rees, M. J. 1978, MNRAS, 184, 61P
Rees, M. J., & Meszaros, P. 1994, ApJL, 430, L93
Rudolph, A., Heinze, J., Fedynitch, A., & Winter, W. 2020, ApJ, 893, 72
Rueda-Becerril, J. M., Mimica, P., & Aloy, M. A. 2014, MNRAS, 438, 1856
Rueda-Becerril, J. M., Mimica, P., & Aloy, M. A. 2015, arXiv:1502.07882
Rybicki, G. B., & Lightman, A. P. 1979, Radiative Processes in Astrophysics (New York: Wiley)
Shidatsu, M., Ueda, Y., Tazaki, F., et al. 2011, PASJ, 63, S785
Sironi, L., Keshet, U., & Lemoine, M. 2015a, SSRv, 191, 519
Sironi, L., Petropoulou, M., & Giannios, D. 2015b, MNRAS, 450, 183
Sironi, L., & Spitkovsky, A. 2009, ApJ, 698, 1523
Sironi, L., & Spitkovsky, A. 2011, ApJ, 726, 75
Sironi, L., Spitkovsky, A., & Arons, J. 2013, ApJ, 771, 54
Spada, M., Ghisellini, G., Lazzati, D., & Celotti, A. 2001, MNRAS, 325, 1559
Stern, B. E., & Poutanen, J. 2008, MNRAS, 383, 1695
Stone, J. M., & Gardiner, T. 2009, NewA, 14, 139
Stone, J. M., Gardiner, T. A., Teuben, P., Hawley, J. F., & Simon, J. B. 2008, ApJS, 178, 137
Tavecchio, F., Landoni, M., Sironi, L., & Coppi, P. 2018, MNRAS, 480, 2872
Tchekhovskoy, A., McKinney, J. C., & Narayan, R. 2009, ApJ, 699, 1789
Tetarenko, A. J., Casella, P., Miller-Jones, J. C. A., et al. 2019, MNRAS, 484, 2987
Toro, E. F. 1999, Riemann Solvers and Numerical Methods for Fluid Dynamics (2nd ed.; Berlin: Springer)
Vincentelli, F. M., Casella, P., Petrucci, P., et al. 2019, ApJL, 887, L19
Vlahakis, N., & Königl, A. 2003, ApJ, 596, 1080
Walker, R. C., Hardee, P. E., Davies, F. B., Ly, C., & Junor, W. 2018, ApJ, 855, 128
Weisskopf, M. C., Soffitta, P., Baldini, L., et al. 2022, JATIS, 8, 026002
Zdziarski, A. A., Lubiński, P., & Sikora, M. 2012, MNRAS, 423, 663
Zdziarski, A. A., Stawarz, Ł., Sikora, M., & Nalewajko, K. 2022a, MNRAS, 515, L17
Zdziarski, A. A., Sikora, M., Pjanka, P., & Tchekhovskoy, A. 2015, MNRAS, 451, 927
Zdziarski, A. A., Tetarenko, A. J., & Sikora, M. 2022b, ApJ, 925, 189
Zhao, G.-Y., Gómez, J. L., Fuentes, A., et al. 2022, ApJ, 932, 72
Zhdankin, V., Werner, G. R., Uzdensky, D. A., & Begelman, M. C. 2017, PhRvL, 118, 055103